Applied Energy 112 (2013) 1115–1125

Contents lists available at SciVerse ScienceDirect

Applied Energy

journal homepage: www.elsevier.com/locate/apenergy

Numerical investigation of the coupled water and thermal management in PEM fuel cell

Tao-Feng Cao, Hong Lin, Li Chen, Ya-Ling He, Wen-Quan Tao *

Key Laboratory of Thermo-Fluid Science and Engineering of MOE, School of Energy and Power Engineering, Xi'an Jiaotong University, Xi'an, China

HIGHLIGHTS

- A fully coupled, non-equilibrium, anisotropic PEM fuel cell computational model is developed.
- The coupled water and heat transport processes are numerically investigated.
- Anisotropic property of gas diffusion layer has an effect on local cell performance.
- The boundary temperature greatly affects the cell local temperature and indirectly influences the saturation profile.
- The cathode gas inlet humidity slightly affects the local temperature distribution.

ARTICLE INFO

Article history:
Received 24 September 2012
Received in revised form 19 January 2013
Accepted 8 February 2013
Available online 25 April 2013

Keywords:
PEM fuel cell
Numerical modeling
Water and thermal management
Thermal boundary conditions
Non-equilibrium phase transfer

ABSTRACT

Water and thermal managements are the most important issue in the operation and optimization of proton exchange membrane fuel cell (PEMFC). A three-dimensional, two-phase, non-isothermal model of PEMFC is presented in this paper. The model is used to investigate the interaction between water and thermal transport processes, the effects of anisotropic characters of gas diffusion layer, different boundary temperature of flow plate and the effect of gas inlet humidity. By comparing the numerical results of different cases, it is found that maximum cell temperature is higher in the isotropic gas diffusion layer; in contrast, the liquid saturation is lower than other case. Moreover, the boundary temperature greatly affects the temperature distribution in PEMFC, and indirectly influences the water saturation distribution. This indicates that the coupled relationship between water and thermal managements cannot be ignored, and these two processes must be considered simultaneously in the optimization of PEMFC.

1. Introduction

The proton exchange membrane fuel cell (PEMFC) has been considered as one of the most promising alterative power sources for automobile engine due to its high energy density and efficiency, low operating temperature and emission. Although, many efforts have been done to improve the performance of the PEMFC over the past decade, the commercialization of PEMFC is still impeded by cost and durability issues [1]. Furthermore, water and thermal management problems have significant impact on the cost, durability and performance of PEMFCs.

Water balance must be ensured in PEMFC operation, because sufficient water is needed for membrane to obtain higher ionic conductivity, however, excess water could cause flooding issue in gas diffusion layer (GDL) and catalyst layer (CL), which directly affects the stability of PEMFC [2]. Meanwhile, thermal management is another important issue since cell temperature influences nearly all kinds of parameters in PEMFC, such as mass diffusion coefficient [3], maximum theoretical voltage and electrochemical activity [4], ionic conductivity [5] and so on. It is more important that the cell temperature impacts the saturation pressure of water, hence, the local drying and flooding in PEMFC components, significantly impact the membrane hydration, so that, the performance and durability of PEMFCs. Furthermore, water and thermal managements are inherently coupled due to the "heat pipe" effect [6].

The water and temperature distributions in a PEMFC depend on many transport phenomena including charge transport, multi-component gas transport, two-phase flow and heat transfer in different components [7]. Due to the strong interaction of these processes and the compact nature of a PEMFC, it is hard to obtain detailed water and temperature data by in situ measurement. In contrast, mathematical simulation is ideally suited to analyzing PEMFC water and heat transport process, especially the interaction between them.

As mentioned by Kandlikar and Lu [7] and Dai et al. [8], though, many non-isothermal and two-phase model are developed in the last decades [6,9–24], only a few of them focus on the coupled

* Corresponding author.
E-mail address: wqtao@mail.xjtu.edu.cn (W.-Q. Tao).

0306-2619/$ - see front matter © 2013 Elsevier Ltd. All rights reserved.
http://dx.doi.org/10.1016/j.apenergy.2013.02.031

Nomenclature

Abbreviation

PEMFC	proton exchange membrane fuel cell
GDL	gas diffusion layer
CL	catalyst layer

Symbols

a	water activity
A	area, m^2
A_s	specific area of catalyst layer, m^{-1}
D	diffusion coefficient, $m^2\ s^{-1}$
F	Faraday's constant, 96,487 C mol^{-1}
i	reaction rate, A m^{-3}
I	average current density, A m^{-2}
K	hydraulic permeability, m^2
R	universal gas constant, 8.314 J mol^{-1} K^{-1}
RH	relative humidity
s	liquid water saturation
T	temperature, K
α	transfer coefficient
ε	porosity
ϕ	potential, V
η	overpotential, V
σ	electrical conductivity, S m^{-1}
ζ	stoichiometric flow ratio
λ	membrane water content

Subscript and superscripts

a	anode
av	average value
c	cathode
d	dissolved
g	gas phase
h	hydrogen
irr	irreversible
k	species
l	liquid
o	oxygen
ref	reference values
rev	reversible
S	source term

effect of water and thermal management. Wang and Wang [16] reported the mechanism of water transport via vapor-phase diffusion under the temperature gradient in two-phase region. Later, Weber and Newman [6] presented a 1-D model to investigate the transport of water due to temperature gradient and the associated effects on cell performance. Their results showed that temperature gradients and thermal management can significantly affect performance and water distribution and fluxes. Recently, Basu et al. [18] highlights the physical characteristics of liquid–vapor phase change and its role in PEMFC operation, and the influence of operating condition on phase change is also examined. A similar work has been done by Khajeh-Hosseini-Dalasm et al. [20]. It was found that the local temperature and saturation greatly affect the phase-change rate. Zamel and Li [19] conducted various parametric studies on temperature distribution in a cathode of a PEMFC.

The above researches are mainly based on the isotropic GDL; nevertheless, the GDL used in PEMFC exhibits strongly anisotropic property [25–27], e.g., permeability, thermal conductivity, and electrical conductivity are highly anisotropic. By now, only several workers integrated the anisotropic property of GDL to their non-isothermal, two-phase model [26,28–30]. Pasaogullari et al. [28] applied a 2-D model to investigate the effects of anisotropy of GDL on temperature and saturation distribution. Bapat and Thynell [29] developed a two-dimensional two-phase model based on the classical two-fluid model to analyze the effect of anisotropic thermal conductivities on the water transport process. He et al. [26] employed a 3-D, two-phase model to investigate the effect of the anisotropic GDL thermal conductivity on the heat transfer and liquid water removal process. Ismail et al. [30] investigated the effect of the anisotropic gas permeability and electrical conductivity of gas GDLs on fuel cell performance. Their results showed that the fuel cell performance was found to be very sensitive to the electrical conductivity but almost insensitive to the gas permeability of the GDL at a realistic range of transport properties. However, there is no such a model which is 3-D, two-phase, non-isothermal and can integrate all the anisotropic properties of GDL.

Furthermore, the former researchers did not pay sufficient attention to the problem of thermal boundary conditions in PEMFC model. Nearly all the researchers assume a constant boundary temperature in their mathematical model. However, many experiments showed that the temperature was not uniform on the back side of flow channel [31–33]. More recently, Yang et al. [34] developed a steady state, multiphase, non-isothermal model with a capillary-extended sub-model in gas channel; water and temperature distributions along the channel as well as their interaction were investigated. However, only the anisotropic thermal conductivity was considered in this model, the anisotropic characters of other properties were ignored.

In this paper, a steady state, three-dimensional, two-phase, non-isothermal model is developed. In order to clearly show the interaction between water and heat transport process, the model fully coupled fluid flow, electrochemical reaction, heat transfer and non-equilibrium phase change processes. Moreover, all the anisotropic properties of GDL are integrated in this model. Detailed mathematical description is presented in the next section, then the effects of anisotropic properties of GDL, boundary temperature and inlet humidity on water and thermal management, especially, the interaction between them are highlighted. Finally, some conclusions are drawn.

2. Model development

2.1. Model assumptions

In order to make the numerical simulation more tractable, some assumptions are made as follows:

(1) The gravity effect is ignored.
(2) The gas mixtures are assumed to be ideal gas.
(3) The liquid water in the gas flow channel is in a mist state, so, the liquid saturation in gas channel is negligible.
(4) Contact resistance between different layers is ignored.
(5) The processes are in steady state.

These assumptions can be easily accepted except the third one. Actually, the gas streams are humidified before feeding to PEM fuel cell. Due to weak thermal management or the water generated in CCL, liquid water normally exists and is removed in the flow channels. Many researchers [35–37] proved that this two-phase flow significantly affect the liquid water transport and removal process

of GDL and CL. However, to exactly simulate this two-phase flow is very complex and computationally demanding. The present research is focused on the coupled water and thermal transport phenomena inside the cathode electrode of PEM fuel cell, typically GDLs and CLs; therefore, to reduce model complexity, a simplified mist assumption is made for the two-phase flow in the channel.

2.2. Model equations

A three-dimensional, two-phase, non-isothermal model is established in this paper, which accounts for the conservation of mass, momentum, species, electrical charge and energy. The governing equations are as follows.

2.2.1. Conservation of mass and momentum

For the gas phase, conservation equations of mass and momentum are:

$$\nabla \cdot (\rho_g \mathbf{u}_g) = S_m \tag{1}$$

$$\nabla \cdot \left(\frac{1}{(\varepsilon^{eff})^2} \rho_g \mathbf{u}_g \mathbf{u}_g \right) = -\nabla p_g + \nabla \cdot \left(\frac{1}{\varepsilon^{eff}} \mu_g \nabla \mathbf{u}_g \right) + S_u \tag{2}$$

In the above equations, ε^{eff} is the effective porosity, which is related to the bulk porosity of the material, ε, and liquid saturation, s, as

$$\varepsilon^{eff} = \varepsilon(1-s) \tag{3}$$

ρ_g is the density of the gaseous mixture, $\mathbf{u}_g$ is velocity vector for the gaseous mixture, and μ_g is the viscosity of the gaseous mixture.

2.2.2. Conservation of species

The conservation equation of each gas species can be described as:

$$\nabla \cdot (\rho_g \mathbf{u}_g \omega_k) = \nabla \cdot (\rho_g D_{k,eff} \nabla \omega_k) + S_k \tag{4}$$

where ω_k is the mass fraction of the kth species, including hydrogen, oxygen and water vapor. D_k^{eff} is the effective mass diffusion coefficient of species k. In gas diffusion layers, D_k^{eff} is determined by

$$D_k^{eff} = f(\varepsilon_{eff}) D_i = \varepsilon_{eff} \left(\frac{\varepsilon_{eff} - 0.11}{1 - 0.11} \right)^{\alpha} D_i \tag{5}$$

where the constant α is 0.521 and 0.785 [38] for in-plane and through-plane diffusions, respectively. In catalyst layer (CL) and gas channel, D_k^{eff} is calculated by

$$D_k^{eff} = \varepsilon_{eff}^{1.5} D_i \tag{6}$$

$$D_i = D_i^0 \left(\frac{p_0}{p} \right)^{1.0} \left(\frac{T}{T_0} \right)^{1.5} \tag{7}$$

2.2.3. Transport of electrical charge

The governing equations for the electrical charge of electron and proton can be written as:

$$\nabla \cdot (\sigma_s \nabla \phi_s) = S_{\phi_s} \tag{8}$$

$$\nabla \cdot (\sigma_m \nabla \phi_m) = S_{\phi_m} \tag{9}$$

where ϕ_s and ϕ_m are the solid phase and electrolyte phase potential. For anisotropic gas diffusion layers, solid phase electrical conductivity σ_s has different value in in-plane and through-plane direction. It is assumed that $\sigma_{s,in} = 10\sigma_{s,th}$ in this paper, and the actual value is listed in Table 2. The membrane electrical conductivity σ_m in S m^{-1} is determined by an empirical correlation [5],

$$\sigma_m = (0.5139\lambda - 0.326) \exp\left[1268 \left(\frac{1}{303} - \frac{1}{T} \right) \right] \tag{10}$$

where λ means membrane water content, which is defined as the number of water molecules per sulfonic acid group within the polymer electrolyte, and will be described later, and T is in K. The source terms S_ϕ and $S_{\phi m}$ are related to volumetric current density in catalyst layers. Considering the agglomerate structure of the catalyst layer, the Bulter–Volmer equation used in this paper is modified by an agglomerate model as follows [39]:

$$i_a = \theta A_s i_{a,ref} \left(\frac{C_h}{C_{h,ref}} \right)^{1/2} \left\{ \exp\left[\frac{\alpha_a n_a F}{RT} \eta_a \right] - \exp\left[-\frac{(1-\alpha_a) n_a F}{RT} \eta_a \right] \right\} \tag{11}$$

$$i_c = \theta A_s i_{c,ref} \frac{C_o}{C_{o,ref}} \left\{ \exp\left[\frac{\alpha_c n_c F}{RT} \eta_c \right] - \exp\left[-\frac{(1-\alpha_c) n_c F}{RT} \eta_c \right] \right\} \tag{12}$$

Here, θ is an effectiveness factor, which is a measure of how readily reactants diffuse through the catalyst agglomerate. The definition of θ can be found in the literature [40].

η_a and η_c refer to over-potential in anode and cathode. They are defined as

$$\eta_a = \phi_s - \phi_m \tag{13}$$

$$\eta_c = V_{oc} - \phi_s + \phi_m \tag{14}$$

The open circuit voltage (in V) is calculated as [41,42],

$$V_{oc} = 1.23 - 0.9 \times 10^{-3} + 2.3 \frac{RT}{4F} \log(p_a^2 p_c) \tag{15}$$

where T is in the unit of K, p_a, p_c is in the unit of atm.

The source terms in Eqs. (1), (2), (4), (8), and (9) are summarized in Table 1. The source term in momentum conservation equation, S_u represents Darcy's drag force imposed by the pore walls on the fluid within the pores, and it usually results in a significant pressure drop across the porous medium. The source term in mass conservation (S_m) and species (S_k) conservation equations are the volumetric sink or source terms due to the electrochemical reactions and phase change in CL or GDL, and they are zero in other parts of the computational domain. The source terms ($S_{\phi s}$, $S_{\phi m}$) in charge conservation equations denote the generation or consumption of electrons and proton in the catalyst layer.

2.2.4. Transport of liquid water

The conservation of liquid water is in terms of liquid saturation, as,

$$\nabla \cdot \left(\rho_l \frac{\eta_g}{\eta_l} \frac{K_{rl}}{K_{rg}} \mathbf{u}_g \right) = \nabla \cdot (\rho_l D_c \nabla s) - S_l \tag{16}$$

where the diffusivity of liquid saturation D_c is expressed as follows:

$$D_c = -\frac{K K_l}{\eta_l} \frac{dp_c}{ds} \tag{17}$$

here K is the absolute permeability. The absolute permeability of GDL is different in in-plane and through-plane direction. According

Table 1
Source terms of different governing equations.

Equation	Source term
Mass	$S_m = S_h + S_o + S_w$
Momentum	$S_u = -\mu_g \mathbf{u}_g / K K_{rg}$
Species	$S_o = -(i_c/4F)M_o$, $S_h = -(i_a/2F)M_h$ $S_w = S_d + S_l$ (in CL), $S_w = S_l$ (in GDL)
Potential	$S_{\phi,s} = -i_a$(in ACL), $S_{\phi,s} = -i_c$ (in CCL) $S_{\phi,m} = -i_a$ (in ACL), $S_{\phi,s} = -i_c$ (in CCL)

to Eq. (17), the liquid saturation diffusivity also has different value in in-plane and through-plane direction.

The capillary pressure p_c is defined as,

$$p_c = p_g - p_l \tag{18}$$

and can be expressed as,

$$p_c = \left(\frac{K}{\varepsilon}\right)^{0.5} \sigma J(s) \tag{19}$$

$$J(s) = \begin{cases} \cos\theta_c[1.417(1-s) - 2.212(1-s)^2 + 1.263(1-s)^3] & \theta_c < 90^o \\ \cos\theta_c[1.417s - 2.212s^2 + 1.263s^3] & \theta_c > 90^o \end{cases} \tag{20}$$

where θ_c is the contact angle of GDL. In reality, the wetting property of GDL is also anisotropic due to the non-uniform distribution of PTFE contents during the coating process. However, the anisotropic nature of wetting property is really complex, and in order to simplify the numerical model, a uniform θ_c is assumed in this paper. The source term S_l denotes the interfacial mass transfer between liquid and water vapor due to evaporation and condensation. It is determined by the following equation [21]:

$$S_l = A_{pore}\frac{Sh_c D_w}{\bar{d}}(1-s)(\rho_w - \rho_{sat})q + A_{pore}\frac{Sh_e D_w}{\bar{d}}s(\rho_w - \rho_{sat}) \times (1-q) \tag{21}$$

where q is a switching function, and it is defined as [43]

$$q = \frac{1 + |(\rho_v - \rho_{sat})|/(\rho_v - \rho_{sat})}{2} \tag{22}$$

In Eq. (21) A_{pore} is the pore surface area per unit volume, D_w is mass diffusivity of water, $\bar{d}$ is characteristic length of water diffusion nearby the evaporation/condensation interface, ρ_{sat} is the saturation water vapor density and is related to the saturation pressure p_{sat}, which is given by the following equation [44]:

$$\log_{10}P_{sat} = -2.1794 + 0.02953T - 9.1837\times10^{-5}T^2 + 1.4454\times10^{-7}T^3 \tag{23}$$

Sh_c and Sh_e are the dimensionless number (Sherwood number) accounting for mass transport capability during condensation or evaporation, respectively, which are calculated as [21]

$$Sh_{ce} = \Gamma_m\Gamma_s\sqrt{\frac{RT}{2\pi M_w}}\frac{\bar{d}}{D_w} \tag{24}$$

here Γ_m is an uptake coefficient that accounts for the combined effects of heat and mass transport limitations in the vicinity of the liquid/vapor interface, and Γ_s is an interfacial area coefficient that is similar to Γ_m. The values of $\bar{d}$ and D_w are not important here since they will be cancel out in Eq. (21).

2.2.5. Transport of dissolved water

Dissolved water is important to the membrane ionic conductivity. The transport of dissolved water in the membrane and catalyst layers is described as,

$$\nabla\cdot(D_w\nabla c_w) - \nabla\cdot\left(n_d\frac{i}{F}\right) = S_d \tag{25}$$

where D_w is the water diffusion coefficient in the membrane phase and is determined by the following equation [5]:

$$D_w = 2.1\times10^{-7}\exp(-2346/T)c_w \tag{26}$$

and n_d is electro-osmotic drag coefficient, and is given by [5]

$$n_d = \frac{2.5\lambda}{22} \tag{27}$$

The source term S_d in the catalyst layer is expressed as follows: In the anode catalyst layer,

$$S_{d,a} = -\gamma_a(c_{w,a} - c^*_{w,a}) \tag{28}$$

In the cathode catalyst layer,

$$S_{d,c} = -\gamma_d(c_{w,c} - c^*_{w,c}) + \frac{i_c}{2F} \tag{29}$$

where C^*_w is the equilibrium water sorption value in the membrane, and is obtained by an empirical expression as follows [5]:

$$c^*_w = \frac{\rho_{mem,dry}}{M_{mem,dry}}\lambda_e \tag{30}$$

where $\rho_{mem,dry}$ and $M_{mem,dry}$ are the density and equivalent weight of a dry proton exchange membrane, respectively. λ_e is the equilibrium membrane water content, and is evaluated by the following empirical formula [5]:

$$\lambda_e = \begin{cases} 0.043 + 17.18a - 39.85a^2 + 36a^3 & (0 < a < 1) \\ 14 + 1.4(a-1) & (1 \leqslant a \leqslant 3) \end{cases} \tag{31}$$

where a is the water vapor activity of vapor in the gas mixture, defined as [45]

$$a = \frac{x_w p}{p_{sat}} \tag{32}$$

γ_a and γ_d are the rate coefficients of the membrane absorption and desorption, respectively, and their values at the anode and cathode catalyst layers are determined by the empirical expression developed by Ge et al. [46].

$$\gamma_a = \frac{1.14\times10^{-5}f_V}{\delta_{cl}}\exp\left[2416\left(\frac{1}{303} - \frac{1}{T}\right)\right] \tag{33}$$

$$\gamma_c = \frac{4.59\times10^{-5}f_V}{\delta_{cl}}\exp\left[2416\left(\frac{1}{303} - \frac{1}{T}\right)\right] \tag{34}$$

here f_v is the volume fraction of water in the electrolyte membrane and it is calculated as

$$f_V = \frac{\lambda V_w}{V_m + \lambda V_w} \tag{35}$$

where V_w and V_w are the molar volumes of water and dry membrane, respectively.

2.2.6. Energy conservation equation

The temperature distribution is important due to the sensitivity of saturation pressure towards to temperature when modeling two-phase phenomena in PEM fuel cell. Hwang and Chen [47] developed a non-dimensional parameter to characterize the degree of local thermal non-equilibrium (LTNE) in fuel cell electrode. It became local thermal equilibrium (LTE) when that parameter is far less than unit. The parameter is 0.018 in the condition of this paper, so that, the LTNE effect is relatively small. Furthermore, for reducing the model complexity, an LTE approximation was employed and the energy conservation equation can be described as,

$$\nabla\cdot(\rho c_p\mathbf{u}_g T) = \nabla\cdot(k_{eff}\nabla T) + S_T \tag{36}$$

where k_{eff} is the effective thermal conductivity, and in porous media it is defined as [44],

$$k_{eff} = -2k_s + (\varepsilon_{eff}/(2k_s + k_g) + (1-\varepsilon_{eff})/3k_s)^{-1} \tag{37}$$

Table 2
Transport property.

Parameter	Value	Reference
Hydrogen diffusion coefficient, $D_{h,ref}$	0.915×10^{-4} m^2 s^{-1}	[49]
Oxygen diffusion coefficient, $D_{o,ref}$	0.22×10^{-4} m^2 s^{-1}	[49]
Water vapor diffusion, $D_{w,ref}$	0.256×10^{-4} m^2 s^{-1}	[49]
Plate electrical conductivity, σ_p	20,000 S m^{-1}	[17]
Plate thermal conductivity, k_p	150 W m^{-1} K^{-1}	[14]
GDL electrical conductivity, σ_{th}, σ_{in}	500,5000 S m^{-1}	[50]
GDL thermal conductivity, $k_{s,th}$, $k_{s,in}$	1.7,21 W m^{-1} K^{-1}	[25]
Membrane thermal conductivity	0.95 W m^{-1} K^{-1}	[13]
GDL gas permeability, $k_{in,p}$, $k_{th,p}$	8.69, 3.0×10^{-12} m^2	[25]
Latent heat, h_{fg}	2.308×10^6 J kg^{-1}	[51]
Liquid water dynamic viscosity, μ_l	3.517×10^{-4} Pa S	[10]
Surface tension, σ	0.0625 N m^{-1}	[10]
Contac angle of GDL, θ_c	110	[17]
Pore surface area per unit volume, A_{pore}	20 m^2/cm^3	[52]
Uptake coefficient, Γ_s	0.001	[21]
Accommodation coefficient, Γ_m	0.01	[21]

The solid phase conductivity k_s in the anisotropic gas diffusion layers exhibits different values in in-plane and through-plane direction and their values are listed in Table 2. In Eq. (37), the liquid water thermal conductivity is not considered, since liquid water thermal conductivity is small compare to the solid phase thermal conductivity of GDL.

The last term in Eq. (36), S_T , represents the heat source of energy conservation equation. Four kinds of heat sources are considered in the current model. They are the reversible heat release during the electrochemical reaction, irreversible heat generation, ohmic heating, and latent heat during condensation, respectively. Thus,

$$S_T = S_{T,rev} + S_{T,act} + S_{T,ohm} + S_{T,con/eva} \tag{38}$$

In the CL all four types of heat source are present and can be described as

$$S_T = i\left(\eta + T\frac{dE}{dT}\right) + \frac{I^2}{\sigma_m} + \frac{I^2}{\sigma_s} + S_l h_{fg} \tag{39}$$

where h_{fg} represents the latent heat of water vapor condensation.

In the GDL both ohmic heating and condensation/evaporation are present. Therefore, the heat source is

$$S_T = \frac{I^2}{\sigma_s} + S_l h_{fg} \tag{40}$$

In the membrane layer the heat source only includes the ohmic heating caused by protonic current flow

$$S_T = \frac{I_m^2}{\sigma_m} \tag{41}$$

In the gas flow channels, the heat sources are simply zero.

3. Numerical implementation

The model equations presented above are discretized by the finite volume method. Then, the algebraic equations are solved iteratively by a self-written code [14,15]. The solution is considered to be convergent when the relative difference of each dependent variable between two consecutive iterations is less than 10^{-5}. The SIMPLE algorithm is utilized to deal with the coupling of the velocity and pressure. The governing equations are assumed to be applicable for all regions throughout the fuel cell. Thus the interfacial conditions at the interfaces of channel/gas diffusion layer, gas diffusion/catalyst layer and catalyst/membrane layer are not needed. Additionally, for the solution of the momentum conservation equation, some tips are employed. A small permeability is set in the porous medium, thus the momentum conservation equation reduces to the extended Darcy's law. While inside a pure fluid region, i.e., gas channel, it recovers the standard Navier–Stokes equation with the porosity being unity and the permeability being infinite. And, the viscosity in the membrane and rib regions is assumed to be infinite in order to ensure a zero fluid velocity in these regions. For the species transport equation, the species mass diffusivity in the membrane is set to zero. Thus non-permeable condition for the species concentration are implemented in the membrane region.

The three-dimensional computational domain of the current model is shown in Fig. 1. Pure hydrogen and oxygen are flowing into the gas channel as a co-flow style. The conventional parallel flow fields are adopted in this model. The model assumes that the fuel cell structure is repeated periodically along the y-direction. Hence, half of a gas channel is taken as the computational domain. The domain includes bipolar plate, gas channel, GDL and CL on both sides and a polymer electrolyte membrane in between. In our previous work [15], the grid-independence test is performed on six grid systems. Finally, a $32 \times 22 \times 40$ ($z \times y \times x$) is chosen considering both accuracy and economics. In this paper, both the computational domain and numerical method are the same to that paper. For convenience, we directly set the grid system in this paper to $32 \times 22 \times 50$ ($z \times y \times x$). Uniform grids are adopted along x and y directions, and a non-uniform grid is used in z direction. Additionally, the model parameters and material properties of each layer are listed in Tables 2 and 3. Cell geometric parameters and operating condition are in Table 4.

The computations were performed with a personal computer with a 3 GHz Intel Dual Core central processor unit, 4 GB RAM,

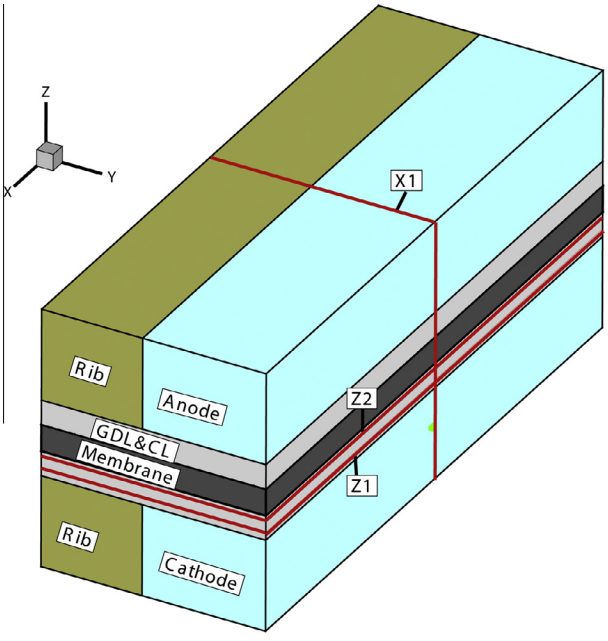

Representative plane	Position
Z1	Middle of cathode GDL
Z2	Middle of cathode CL
X1	1/2 of channel length

Fig. 1. Computational domain and representative plane.

Table 3
Model parameters.

Parameter	Value	Reference
Anode exchange current density multiply specific area, $A_s i_{a,ref}$	5.0×10^7 A m^{-3}	[14]
Cathode exchange current density multiply specific area, $A_s i_{c,ref}$	120 A m^{-3}	[14]
Reference concentration, $c_{h,ref}$, $c_{h,ref}$	56.4, 3.39 mol m^{-3}	[42]
Anode transfer coefficient, α_a	0.5	[13]
Cathode transfer coefficient, α_c	0.5	[13]
Porosity ε_{gdl}, ε_{cl}	0.6, 0.28	[14,51]
Faraday's constant	96,487 C mol^{-1}	[13]

Table 4
Cell geometric parameters and operating condition.

Parameter	Value	Reference
Gas channel length	0.05 m	
Gas channel width	1×10^{-3} m	
Gas channel height	1×10^{-3} m	
Land width	1×10^{-3} m	
Thickness of gas diffusion layer	2.54×10^{-4} m	[24]
Thickness of catalyst layer	2.87×10^{-5} m	[24]
Thickness of membrane	2.3×10^{-4} m	[24]
Anode/cathode pressure, p_a/p_c	1/1 atm	[53]
Inlet gas stoichiometric ratio, ζ_a/ζ_c	2/2	[17]
Inlet gas temperature, T_{in}	353 K	[14]

and the Windows 7 operating system. Typically, The CPU time is about 5 h for running a case.

3.1. Boundary conditions

At the inlet of gas flow channels, the temperature and gas species concentrations are specified. The inlet velocities are specified by

$$u_{a,in} = \zeta_a \frac{I_{ref}}{2F} A_m \frac{RT_{a,in}}{p_{a,in}} \frac{1}{w_{h,in}} \frac{1}{A_{ch}} \tag{42}$$

$$u_{c,in} = \zeta_c \frac{I_{ref}}{4F} A_m \frac{RT_{c,in}}{p_{c,in}} \frac{1}{w_{o,in}} \frac{1}{A_{ch}} \tag{43}$$

where ζ_a and ζ_c are the reactant stoichiometric flow ratio of the anode and cathode, respectively, and they are defined at the reference current density of 1.0 A in this work. A_m is actual active area of the membrane which is equivalent to the surface area of gas diffusion layer and A_{ch} is the cross-sectional area of the gas channel.

At the outlet of gas flow channels, the local one-way assumption is adopted for all the variables, and the outlet velocity is corrected by a global mass conservation constraint [48].

For the boundary of x–z plane, symmetrical conditions are adopted. That is, the gradient in the y-direction of each variable is zero.

At the solid surface, the no-slip condition is applied for the velocity and non-permeable condition for the species mass fraction.

For the liquid saturation, the gradient of liquid saturation is set to zero at the interface between the gas channel and the diffusion layer.

For the electrical charge equations, the boundary conditions are described as follows:

At the outer surface of the anode channel,

$$\phi_{s,a} = 0, \quad \frac{\partial \phi_m}{\partial z} = 0 \tag{44}$$

At the outer surface of the cathode channel,

$$\phi_{s,c} = V_{cell}, \quad \frac{\partial \phi_m}{\partial z} = 0 \tag{45}$$

At other surfaces,

$$\frac{\partial \phi_s}{\partial \boldsymbol{n}} = 0, \quad \frac{\partial \phi_m}{\partial \boldsymbol{n}} = 0 \tag{46}$$

4. Results and discussion

In order to investigate the effect of anisotropic property of GDL on water and thermal management and clearly understand the coupled phenomena between water transport and heat transfer process, four different cases are simulated by the model presented above. The computational conditions are listed in Table 5. For revealing water and thermal interaction more obviously, the simulated results of 0.4 V is discussed as follows.

4.1. Temperature distribution and the influence of anisotropic gas diffusion layer

Figs. 2 and 3 display the temperature profile at plane $X1$ and $Z1$. It can be seen that the temperature under the region of channel is higher than that under the rib region. This is because current collector rib has a high thermal conductivity compared with gas mixtures in gas channel. It means that heat generated under the rib region can be quickly removed through the current collector rib; however, the heat generated under the channel region cannot be easily removed by the gas flow. This indicates that heat generated in CL and GDL is mainly removed through current collect rib to cooling channel. In addition, from Fig. 2 it can be seen that the temperature in the cathode side is higher than that of the anode side. This is due to the heat generated by electrochemical reaction and water vapor condensation process. From Fig. 3, it is found that the temperature increases along the flow direction. This is because the inlet cell temperature is fixed to 353 K, and the exothermic electrochemical reaction is conducted along the flow direction.

For the anisotropic case, the property of GDL in through-plane (z-direction) and in-plane direction (x- and y-direction) is different, as indicated in Table 2. Moreover, for the isotropic case, the property of GDL is the same in x, y, z-direction, and the value is based on the through-plane one of the anisotropic case.

The influence of anisotropic GDL on heat remove process can be seen in Figs. 2b and 3b. It is found that both the maximum temperature and temperature profile are different from isotropic case. The maximum temperature (357 K) in the isotropic GDL is about 1 K higher than that (356.2 K) in the anisotropic GDL. This is mainly because the in-plane thermal conductivity in the isotropic GDL is much lower than that in the anisotropic GDL. Also, due to the large in-plane thermal conductivity in the anisotropic GDL, the temperature gradient in y-direction is much smaller in the anisotropic GDL than that in isotropic GDL. This phenomenon can also be found in Figs. 3a and 3b. The difference in temperature distribu-

Table 5
Different cases for simulation.

	GDL property	Gas humidity at anode/cathode inlet	Boundary temperature (K)
Case 1	Isotropic	1.0/0.2	353
Case 2	Anisotropic	1.0/0.2	353
Case 3	Anisotropic	1.0/0.2	Linearly increase from 350 at inlet to 355 at outlet
Case 4	Anisotropic	1.0/1.0	353

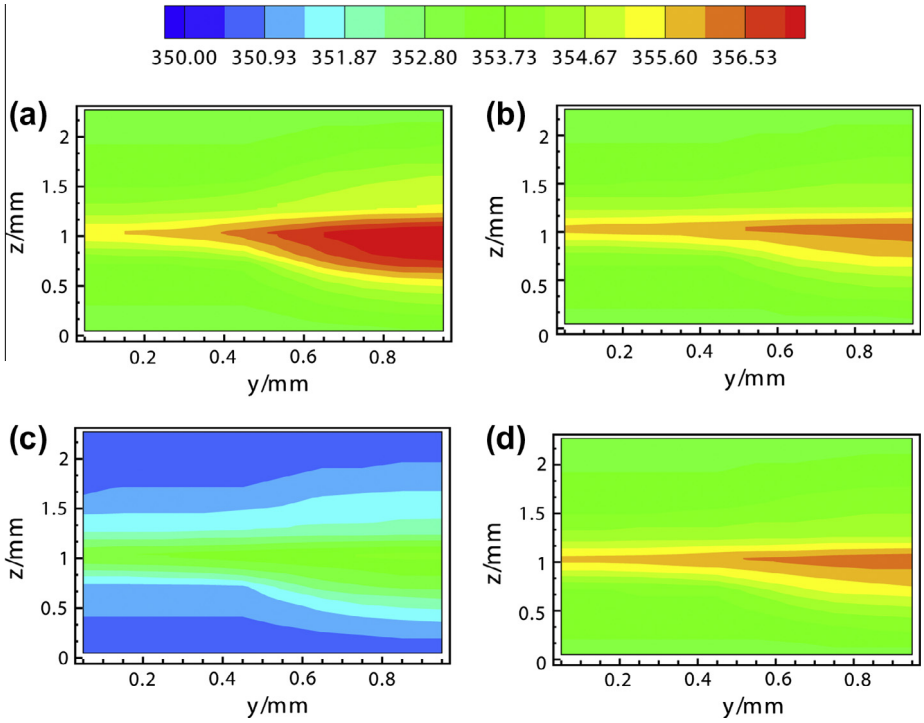

Fig. 2. Temperature distribution (K) at plane *X*1: (a) isotropic GDL, (b) anisotropic GDL, (c) effect of boundary temperature, and (d) effect of inlet humidity.

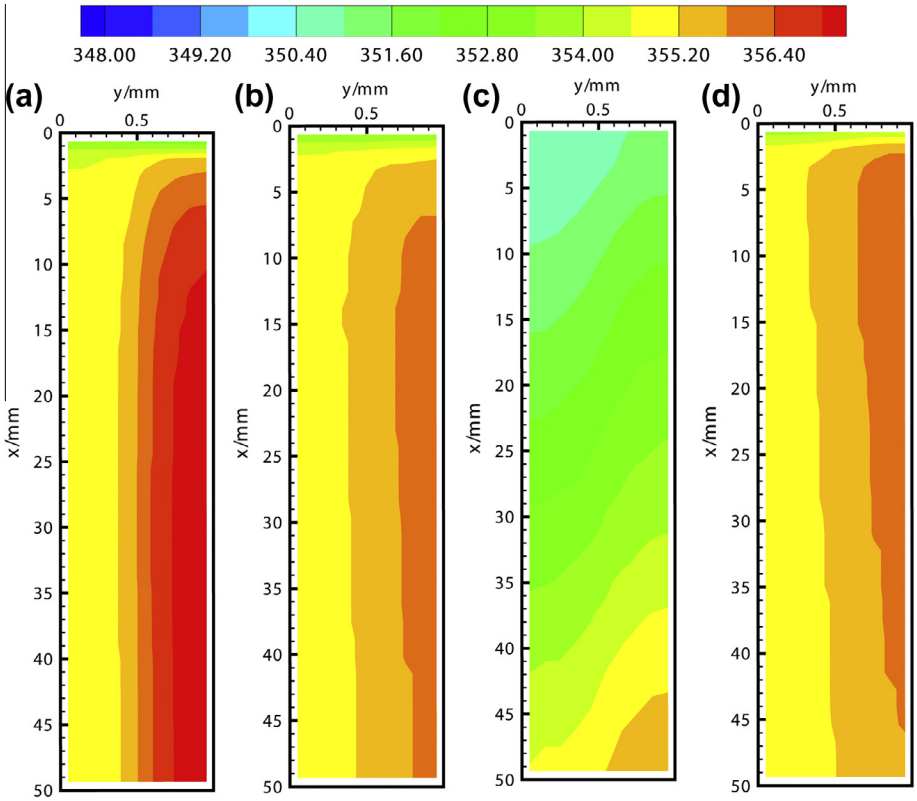

Fig. 3. Temperature distribution (K) at plane *Z*1: (a) isotropic GDL, (b) anisotropic GDL, (c) effect of boundary temperature, and (d) effect of inlet humidity.

tions between the isotropic and anisotropic GDL further proves the heat in CL and GDL is removed by conductivity from channel rib.

Lee et al. [54] experimentally studied the temperature distribution across a proton exchange membrane fuel cell by inserting micro-thermocouples between a gas diffusion layer and membrane electrode assembly. Their results showed a 2 K temperature increase from cathode channel/GDL interface to CL/GDL interface. From our numerical results, a temperature difference of 3 K was

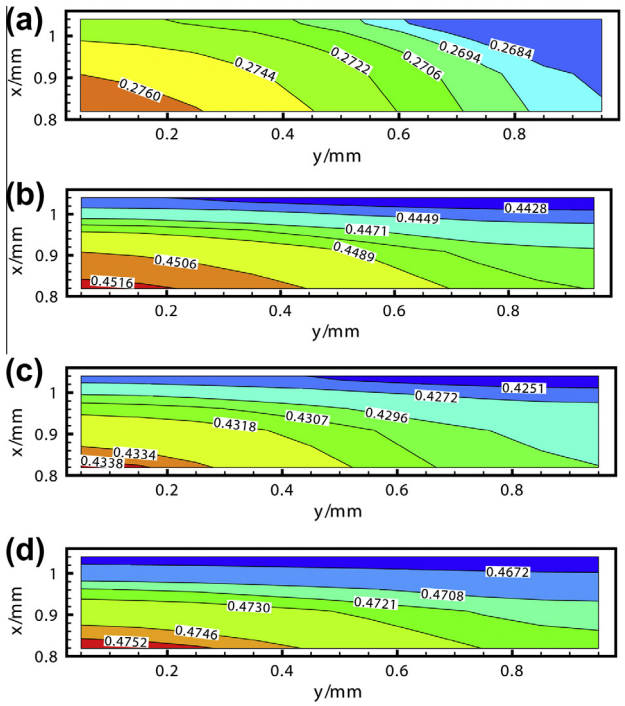

Fig. 4. Cathode electrode water saturation distribution at plane *X*1: (a) isotropic GDL, (b) anisotropic GDL, (c) effect of boundary temperature, and (d) effect of inlet humidity.

found at the cross section in the anisotropic case, and 4 K was found in the isotropic case. Compared with the experiment result, it is found that the temperature distribution of the anisotropic case is closer to the experiment results.

4.2. Liquid saturation distribution

Water in PEMFC comes from the water vapor in humid gas and the oxygen reduction reaction (ORR). However, the state of the produced water in the cathode catalyst layer by ORR is still an argument in the literature. In this paper, it is assumed that water generated in the catalyst surface is in the form of dissolved water and then converts to gas phase. In this case, the liquid water in CL and GDL comes from water vapor condensation process rather than ORR. The condensation process occurred when water vapor partial pressure is larger than water saturate pressure which is greatly affected by temperature.

The liquid water saturation of different cases is shown in Figs. 4 and 5. From Fig. 4, it is found that the liquid water saturation increases from the catalyst/membrane interface to the gas diffusion layer/channel interface. It also can be seen that a relative high water saturation region exits near the current collector rib. According to temperature distribution in Fig. 2, it can be seen that the low water saturation area is corresponding to the high temperature area which means high water saturation pressure; and the high water saturation area is corresponding to the low temperature area which means high water saturation pressure. In other words, less water vapor condenses in the high temperature region which near the membrane catalyst layer interface. In contrast, more water vapor condenses in the low temperature region which near the current collector rib. This phenomenon indicates a water transport mechanism via temperature gradient. From Fig. 5, it can be seen that the water saturation increases along the flow direction from inlet to outlet. The reason includes the following two aspects. For one hand, the water vapor partial pressure is increased along the flow direction due to the accumulation of water vapor. It means that the water condensation rate is increased along the flow direction. In other hand, liquid water flows from inlet to outlet by shear force.

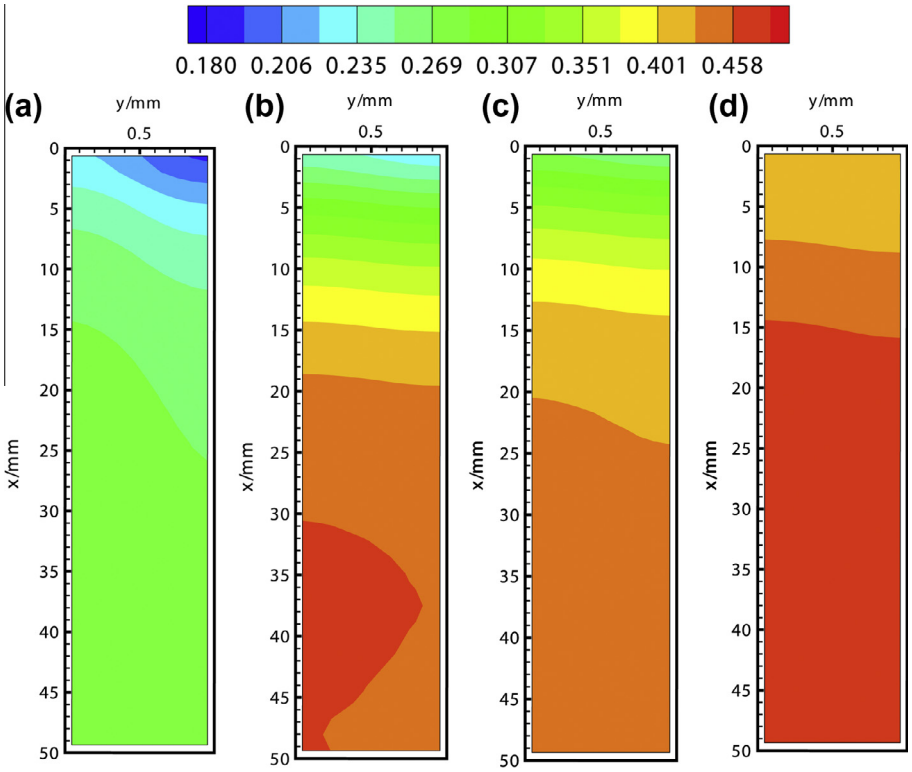

Fig. 5. Cathode electrode water saturation distribution at plane *Z*1: (a) isotropic GDL, (b) anisotropic GDL, (c) effect of boundary temperature, and (d) effect of inlet humidity.

4.2.1. Influence of anisotropic GDL

By comparing Figs. 4a and 4b, it is found that both the saturation level and profile are different in the isotropic and anisotropic cases. The water saturation in the isotropic case is lower than that of the anisotropic case. This is mainly because the temperature in the isotropic GDL is higher. And the higher temperature leads to a higher saturation pressure and much more water exists in vapor phase. Moreover, the saturation profile along *y*-direction is more uniform in the anisotropic case. The reason can be explained as, in one hand, the temperature profile of anisotropic case is more uniform in *y*-direction as indicated in Fig. 2b; in other hand, the liquid saturation diffusivity is large in the in-plane direction due to the large permeability of GDL at in-plane direction.

4.2.2. Influence of boundary temperature

The temperature of the flow plate is a tradeoff between heat generation rate in electrode and heat removing ability of cooling channel and often exhibits a non-uniform distribution as indicated in Section 1. In reality, the temperature profile of flow plate is significantly affected by cooling conditions. However, it is difficult to determine accurately the temperature distribution of the plates. To simply simulate this non-uniform temperature distribution of flow plate, it is assumed that both the anode and cathode boundary temperatures linearly increase from 350 K at inlet to 355 K at outlet. Compared with the constant boundary temperature at 353 K, this temperature profile means a cooling process in inlet region and heating process in the outlet region.

Under this temperature boundary condition, the temperature distributions at planes *X*1 and *Z*1 are displayed in Figs. 2c and 3c, respectively. From Fig. 3c, it is found that the temperature increases slowly from inlet to outlet. However, under the constant temperature boundary condition, the temperature raises quickly at the very beginning of channel inlet. It means that the boundary temperature greatly affects the temperature profile inside the PEMFC.

Attention is now turned to the liquid water distribution shown in Fig. 5c. Compared with Fig. 5b, the saturation level is slightly increased in inlet region, and decreased in the outlet region. According to the temperature profile in Fig. 3c, the variation of saturation level in this case can be easily understood. The reason is because that the lower boundary temperature at the inlet results into the condensation of water vapor presented in the incoming gas stream, then the slightly incensement of saturation level in the inlet region. It means that temperature boundary condition indirectly influence the saturation profile.

4.2.3. Influence of gas humidity

By increasing gas inlet humidity, the influence of humidity on water saturation is studied. The results are shown in Figs. 4d and 5d. It is found that the water saturation level becomes high in this case, especially in the inlet region. With the increase of gas humidity, more water vapor flows into the cell with gas mixture. It means that the water vapor partial pressure is increased. In other words, the capability of carrying water vapor of gas mixture is decreased with the increase of gas humidity. Therefore, more water condenses to liquid phase, and then the water saturation is increased. Moreover, the gas is fully humidified, so water vapor condensation occurs immediately when gas flows into gas channel, this leads to the much higher saturation level of the inlet region. In other hands, the heat released in the condensation process will cause the increase of cell temperature; and then slow down the condensation process. Finally, a dynamic equilibrium will be reached between the condensation/evaporation processes.

Then turn attention to Fig. 3d. It is found that the temperature is indeed increased slightly in the gas inlet region. This is caused of the heat released from vapor condensation process.

From the above results, it can be concluded that temperature profile greatly affects the liquid water saturation level and local distribution; liquid water also has an influence on temperature distribution. This indicates that water and thermal managements are indeed inherently coupled with each other, and also proves that they must be considered simultaneously in the optimization process of PEMFC.

4.3. The effect of anisotropic properties on cell performance

4.3.1. Polarization curves

A comparison of polarization curves for case 1 and case 2 are displayed in Fig. 6. Clearly, it is found that in low current density region (<0.3 A cm^{-2}), the two cases exhibit nearly the same performance. The reason can be attributed to that the voltage lose in low current density regions is mainly activation lose. With the increase of current density, Ohmic lose and mass transport lose become important, and the mass diffusivity and electronic conductivity are higher in the anisotropic cases. It leads to a smaller voltage lose of the anisotropic cases in a relative higher current density. As a result, a relative higher cell performance is found in the higher current density region.

4.3.2. Local gas distribution

The effective diffusion coefficient of species in a fibrous porous structure is defined in Eq. (5). In the current model, the porosity of GDL is 0.6, and then, $f(\varepsilon_{eff})$ is about 0.277 in the through-plane direction, but 0.347 in the in-plane direction. Figs. 7a and 7b displays the distribution of oxygen mass fraction in cathode electrode of plane *X*1. Compare Figs. 7a and 7b, the oxygen mass fraction in the region under rib of the anisotropic GDL is relatively higher than that in the isotropic GDL. Minimum oxygen mass fraction is about 0.05 in isotropic case, but 0.25 in anisotropic case. Also, a uniform oxygen mass fraction distribution is shown in the anisotropic GDL. The reason is that the in-plane effective diffusivity of oxygen for the anisotropic GDL is larger than that for the isotropic GDL, more oxygen can diffuse to the under rib region; furthermore, the isotropic case has a relatively higher current density under rib region than the anisotropic case as can be seen in Figs. 8a and 8b, this means that more oxygen is consumed under rib in the isotropic case.

4.3.3. Local current density distribution

The local current density distribution at plane *Z*2 is displayed in Fig. 8. From Eq. (12), it can be deduced that the ultimate profile of current density is determined by the combined effects of oxygen

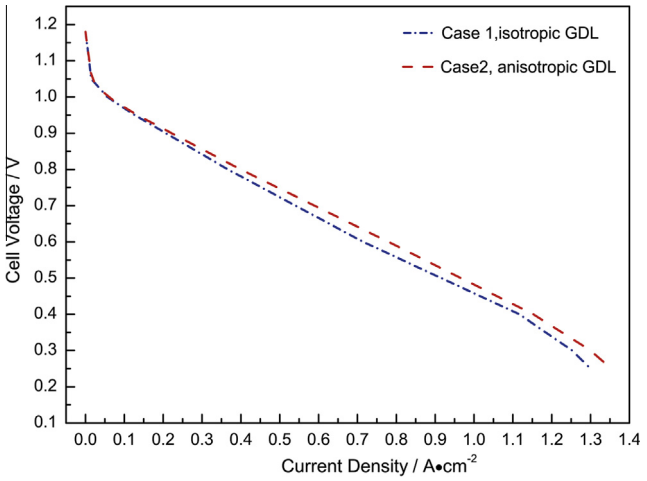

Fig. 6. Polarization curve of isotropic and anisotropic cases.

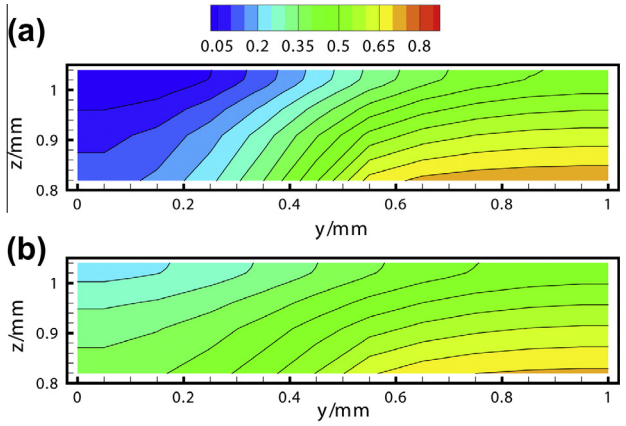

Fig. 7. Cathode electrode oxygen mass fraction at plane X1: (a) isotropic GDL and (b) anisotropic GDL.

concentration and over-potential changes. From Fig. 7, the mass fraction is higher under the channel region than that under the rib; however, from Fig. 8a, it is found that the current density is larger in the under rib region. It means that, the over-potential plays a more important role than oxygen concentration in the determination of the current density in cathode catalyst layer. In contrast, a qualitatively opposite profile of local current density distribution is found in the anisotropic case, as displayed in Fig. 8b. The current density under channel region is slightly higher than that under the rib. This is mainly caused by the large transport coefficient in the anisotropic GDL in-plane direction.

Wang and Liu [55] directly measured the current densities under the channel and the shoulder in PEM fuel cells separately. Their experimental results showed that the current density produced under the channel is slightly higher than that under the shoulder at 0.4 V and 1 atm. Compared the numerically simulated current density distribution to the experimental results, it can be found that the current density distribution of the anisotropic case agrees well to the experimental results. While the isotropic case predicts a wrong distribution.

The effect of temperature boundary condition is shown in Fig. 8c. It is found interestingly that the increase of saturation level at inlet region does not cause the decrease of current density; rather, the current density is increased. Actually, liquid water not only prevents the oxygen diffuse to the catalyst layer, but also increases the water content of the membrane. It means that, in one hand, liquid water plays the role of reducing current; however, in other hand, liquid water plays the role of increasing current. The increase of current density indicates that the role of membrane hydration by liquid water is more important in this case. Together with the liquid water saturation profile displayed in Fig. 5c, it is found that cooling inlet region and heating outlet region has a positive influence on cell performance.

Finally, from Fig. 8d, a worse cell performance is found under fully humidified gas, especially in the outlet region. According to the liquid saturation level in Fig. 5d, it can be concluded that the reduction of current density is caused by the flooding water.

5. Conclusion

In this paper, a three-dimensional, two-phase, non-isothermal proton exchange membrane (PEMFC) model is developed. The model fully coupled the transport processes and electrochemical reaction, and also integrated the anisotropic property of gas diffusion layer (GDL). With this model, the influence of anisotropic GDL, temperature boundary condition and inlet humidity on water and thermal management are numerically investigated. The coupled effect of water and thermal managements are carefully analyzed. From the numerical simulation results, the following conclusions can be obtained:

(1) The profile of temperature and liquid water saturation are greatly different between the isotropic and the anisotropic GDL; in addition, for the isotropic case, the maximum temperature is higher, however, the saturation level of the cath-

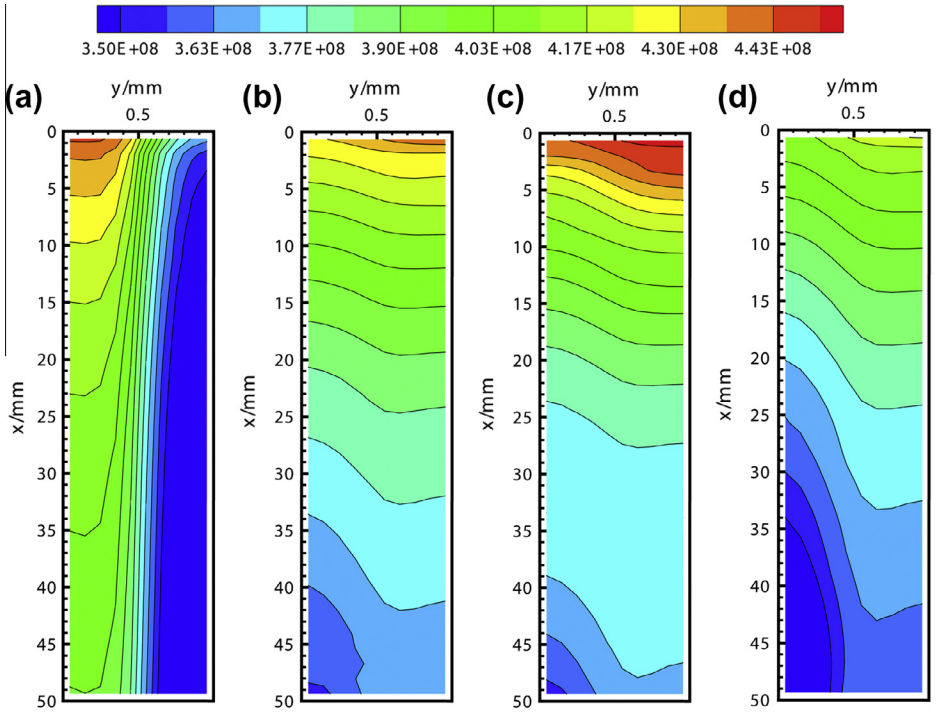

Fig. 8. Local current density distribution (A m^{-3}) at plane *Z*2: (a) isotropic GDL, (b) anisotropic GDL, (c) effect of boundary temperature, and (d) effect of inlet humidity.

ode GDL is much lower. Therefore, the assumption of isotropic property of GDL will overestimate cell temperature and underestimate saturation level.

(2) The temperature boundary condition greatly affects the cell local temperature distribution and indirectly influences the saturation profile. The numerical results indicate that with a heat management strategy of cooling inlet region and heating outlet region, a good cell performance can be reached.

(3) By increasing the gas inlet relative humidity, the saturation level of cathode GDL is increased, and the inlet region temperature is also increased slightly.

(4) Modeling with anisotropic properties predict more accurate current density and temperature distributions than that of isotropic properties.

Acknowledgements

This work was supported by the Key Project of National Natural Science Foundation of China (No. 51136004) and the National Basic Research Program of China (973 Program) (2011CB707203).

References

[1] de Bruijn FA. PEM fuel cells for transport applications: state of the art and challenges. AIP Conf Proc 2009:3–12.
[2] Li H, Tang YH, Wang ZW, Shi Z, Wu SH, Song DT, et al. A review of water flooding issues in the proton exchange membrane fuel cell. J Power Sources. 2008;178:103–17.
[3] Stockie JM, Promislow K, Wetton BR. A finite volume method for multicomponent gas transport in a porous fuel cell electrode. Int J Numer Methods Fluids 2003;41:577–99.
[4] Faghri A, Guo Z. Challenges and opportunities of thermal management issues related to fuel cell technology and modeling. Int J Heat Mass Transfer 2005;48:3891–920.
[5] Springer TE, Zawodzinski TA, Gottesfeld S. Polymer electrolyte fuel cell model. J Electrochem Soc 1991;138:2334–42.
[6] Weber AZ, Newman J. Coupled thermal and water management in polymer electrolyte fuel cells. J Electrochem Soc 2006;153:A2205.
[7] Kandlikar SG, Lu Z. Fundamental research needs in combined water and thermal management within a proton exchange membrane fuel cell stack under normal and cold-start conditions. J Fuel Cell Sci Technol 2009;6:044001.
[8] Dai W, Wang HJ, Yuan XZ, Martin JJ, Yang DJ, Qiao JL, et al. A review on water balance in the membrane electrode assembly of proton exchange membrane fuel cells. Int J Hydrogen Energy 2009;34:9461–78.
[9] Dutta SSS. Numerical prediction of temperature distribution in PEM fuel cells. Numer Heat Transfer Part A: Appl 2000;38:111–28.
[10] Wang ZH, Wang CY, Chen KS. Two-phase flow and transport in the air cathode of proton exchange membrane fuel cells. J Power Sources 2001;94:40–50.
[11] Djilali N, Lu D. Influence of heat transfer on gas and water transport in fuel cells. Int J Therm Sci 2002;41:29–40.
[12] Berning T, Djilali N. Three-dimensional computational analysis of transport phenomena in a PEM fuel cell – a parametric study. J Power Sources 2003;124:440–52.
[13] Ju H, Meng H, Wang CY. A single-phase, non-isothermal model for PEM fuel cells. Int J Heat Mass Transfer 2005;48:1303–15.
[14] Tao WQ, Min CH, Liu XL, He YL, Yin BH, Jiang W. Parameter sensitivity examination and discussion of PEM fuel cell simulation model validation: Part I. Current status of modeling research and model development. J Power Sources 2006;160:359–73.
[15] Min CH, He Y, Liu XL, Yin BH, Jiang W, Tao WQ. Parameter sensitivity examination and discussion of PEM fuel cell simulation model validation: Part II: results of sensitivity analysis and validation of the model. J Power Sources 2006;160:374–85.
[16] Wang Y, Wang C-Y. A nonisothermal, two-phase model for polymer electrolyte fuel cells. J Electrochem Soc 2006;153:A1193.
[17] Luo G, Ju H, Wang CY. Prediction of dry–wet–dry transition in polymer electrolyte fuel cells. J Electrochem Soc 2007;154:B316–21.
[18] Basu S, Wang CY, Chen KS. Phase change in a polymer electrolyte fuel cell. J Electrochem Soc 2009;156:B748–56.
[19] Zamel N, Li X. Non-isothermal multi-phase modeling of PEM fuel cell cathode. Int J Energy Res 2009:568–84.
[20] Khajeh-Hosseini-Dalasm N, Fushinobu K, Okazaki K. Phase change in the cathode side of a proton exchange membrane fuel cell. J Power Sources 2010;195:7003–10.
[21] Wu H, Berg P, Li X. Steady and unsteady 3D non-isothermal modeling of PEM fuel cells with the effect of non-equilibrium phase transfer. Appl Energy 2010;87:2778–84.
[22] Perng S-W, Wu H-W. Non-isothermal transport phenomenon and cell performance of a cathodic PEM fuel cell with a baffle plate in a tapered channel. Appl Energy 2011;88:52–67.
[23] Ramos-Alvarado B, Hernandez-Guerrero A, Ellis MW. Non-equilibrium two-phase model of the air-cathode of a PEM fuel cell based on GDL experimental water transport characteristics. J Power Sources 2012.
[24] Liu X, Lou G, Wen Z. Three-dimensional two-phase flow model of proton exchange membrane fuel cell with parallel gas distributors. J Power Sources 2010;195:2764–73.
[25] Yang WW, Zhao TS, He YL. Modelling of coupled electron and mass transport in anisotropic proton-exchange membrane fuel cell electrodes. J Power Sources 2008;185:765–75.
[26] He G, Yamazaki Y, Abudula A. A three-dimensional analysis of the effect of anisotropic gas diffusion layer (GDL) thermal conductivity on the heat transfer and two-phase behavior in a proton exchange membrane fuel cell (PEMFC). J Power Sources 2010;195:1551–60.
[27] Zamel N, Li X, Shen J. Numerical estimation of the effective electrical conductivity in carbon paper diffusion media. Appl Energy 2012;93:39–44.
[28] Pasaogullari U, Mukherjee PP, Wang CY, Chen KS. Anisotropic heat and water transport in a PEFC cathode gas diffusion layer. J Electrochem Soc 2007;154:B823.
[29] Bapat CJ, Thynell ST. Effect of anisotropic thermal conductivity of the GDL and current collector rib width on two-phase transport in a PEM fuel cell. J Power Sources 2008;179:240–51.
[30] Ismail MS, Hughes KJ, Ingham DB, Ma L, Pourkashanian M. Effects of anisotropic permeability and electrical conductivity of gas diffusion layers on the performance of proton exchange membrane fuel cells. Appl Energy 2012;95:50–63.
[31] Hakenjos A, Muenter H, Wittstadt U, Hebling C. A PEM fuel cell for combined measurement of current and temperature distribution, and flow field flooding. J Power Sources 2004;131:213–6.
[32] Wang MH, Guo H, Ma CF. Temperature distribution on the MEA surface of a PEMFC with serpentine channel flow bed. J Power Sources 2006;157:181–7.
[33] Lin H, Cao T-F, Chen L, He Y-L, Tao W-Q. In situ measurement of temperature distribution within a single polymer electrolyte membrane fuel cell. Int J Hydrogen Energy 2012;37:11871–86.
[34] Yang X-G, Ye Q, Cheng P. Matching of water and temperature fields in proton exchange membrane fuel cells with non-uniform distributions. Int J Hydrogen Energy 2011;36:12524–37.
[35] Berning T, Odgaard M, Kær SK. A computational analysis of multiphase flow through PEMFC cathode porous media using the multifluid approach. J Electrochem Soc 2009;156:B1301.
[36] Gurau V, Mann JA. Effect of interfacial phenomena at the gas diffusion layer-channel interface on the water evolution in a PEMFC. J Electrochem Soc 2010;157:B512.
[37] Chen L, Luan H-B, He Y-L, Tao W-Q. Pore-scale flow and mass transport in gas diffusion layer of proton exchange membrane fuel cell with interdigitated flow fields. Int J Therm Sci 2012;51:132–44.
[38] Pharoah JG, Karan K, Sun W. On effective transport coefficients in PEM fuel cell electrodes: anisotropy of the porous transport layers. J Power Sources 2006;161:214–24.
[39] Wang CY. Fundamental models for fuel cell engineering. Chem Rev 2004;104:4727–65.
[40] Liu X, Tao W, Li Z, He Y. Three-dimensional transport model of PEM fuel cell with straight flow channels. J Power Sources 2006;158:25–35.
[41] Bernardi DM, Verbrugge MW. Mathematical model of a gas diffusion electrode bonded to a polymer electrolyte. AICHE J 1991;37:1151–63.
[42] Bernardi DM, Verbrugge MW. A mathematical model of the solid-polymer-electrolyte fuel cell. J Electrochem Soc 1992;139:2477.
[43] He W, Yi JS, Van Nguyen T. Two-phase flow model of the cathode of PEM fuel cells using interdigitated flow fields. AICHE J. 2000;46:2053–64.
[44] Gurau V, Liu H, Kakac S. Two dimensional model for proton exchange membrane fuel cells. AICHE J. 1998;44:2410–22.
[45] Sun H, Liu H, Guo L-J. PEM fuel cell performance and its two-phase mass transport. J Power Sources 2005;143:125–35.
[46] Ge S, Li X, Yi B, Hsing IM. Absorption, desorption, and transport of water in polymer electrolyte membranes for fuel cells. J Electrochem Soc 2005;152:A1149.
[47] Hwang JJ, Chen PY. Heat/mass transfer in porous electrodes of fuel cells. Int J Heat Mass Transfer 2006;49:2315–27.
[48] Tao WQ. Numerical heat transfer. Xi'an: Xi'an Jiaotong University Press; 2001.
[49] Berning T, Lu DM, Djilali N. Three-dimensional computational analysis of transport phenomena in a PEM fuel cell. J Power Sources 2002;106:284–94.
[50] Meng H, Wang CY. Electron transport in PEFCs. J Electrochem Soc 2004;151:A358–67.
[51] Wu H, Li X, Berg P. On the modeling of water transport in polymer electrolyte membrane fuel cells. Electrochim Acta 2009;54:6913–27.
[52] Kumbur EC, Sharp KV, Mench MM. Validated Leverett approach for multiphase flow in PEFC diffusion media. J Electrochem Soc 2007;154:B1295.
[53] Mazumder S, Cole JV. Rigorous 3-D mathematical modeling of PEM fuel cells. J Electrochem Soc 2003;150:A1510.
[54] Lee S-K, Ito K, Ohshima T, Noda S, Sasaki K. In situ measurement of temperature distribution across a proton exchange membrane fuel cell. Electrochem Solid-State Lett 2009;12:B126.
[55] Wang L, Liu H. Separate measurement of current density under the channel and the shoulder in PEM fuel cells. J Power Sources 2008;180:365–72.